

# Effect of Bed Clay on Surface-Water Wave Reconstruction from Ripples

Jonathan Malarkey<sup>1</sup>, Ellen Pollard<sup>2</sup>, Roberto Fernández<sup>3</sup>, Xuxu WU<sup>4</sup>, Jaco H. Baas<sup>1</sup>, and Daniel R. Parsons<sup>5</sup>

<sup>1</sup>Bangor University

<sup>2</sup>Energy and Environment Institute, University of Hull

<sup>3</sup>Department of Civil and Environmental Engineering, The Pennsylvania State University

<sup>4</sup>University of Hull

<sup>5</sup>Loughborough University

April 08, 2024

## Abstract

Wave ripples can provide valuable information on their formative hydrodynamic conditions in past subaqueous environments by inverting dimension predictors. However, these inversions do not usually take the mixed non-cohesive and cohesive nature of sediment beds into account. Recent experiments involving sand–kaolinite mixtures have demonstrated that wave-ripple dimensions and the threshold of motion are affected by bed clay content. Here, a clean-sand method to determine wave climate based on orbital ripple wavelength has been adapted to include the effect of clay and a consistent shear-stress threshold parameterisation. Based on present-day examples with known wave conditions, the results show that the largest clay effect occurs for coarse sand with median grain diameters over 0.45 mm. For a 7.4% volumetric clay concentration, the range of possible water-surface wavelengths and water depths can be reduced significantly, by a factor of three and four, respectively, compared to clean sand.

## Hosted file

malarkey\_Supporting\_information.docx available at <https://authorea.com/users/545296/articles/741327-effect-of-bed-clay-on-surface-water-wave-reconstruction-from-ripples>

# Effect of Bed Clay on Surface Water-Wave Reconstruction from Ripples

Jonathan Malarkey<sup>1</sup>, Ellen M. Pollard<sup>2</sup>, Roberto Fernández<sup>3</sup>, Xuxu Wu<sup>2,4</sup>, Jaco H. Baas<sup>1</sup>  
and Daniel R. Parsons<sup>5</sup>

<sup>1</sup>School of Ocean Sciences, Bangor University, Menai Bridge, Anglesey LL59 5AB, UK.

<sup>2</sup>Energy and Environment Institute, University of Hull, Hull, HU6 7RX, UK.

<sup>3</sup>Department of Civil and Environmental Engineering, The Pennsylvania State University, State College, PA 16802, USA.

<sup>4</sup>School of Environmental Sciences, University of Hull, Hull, HU6 7RX, UK.

<sup>5</sup>Department of Geography and Environment, Loughborough University, Loughborough, LE11 3TU, UK.

Corresponding author: Jonathan Malarkey ([j.malarkey@bangor.ac.uk](mailto:j.malarkey@bangor.ac.uk))

## Key Points:

- Wave-ripple dimensions provide important information on past subaqueous environments
- Here, a clean-sand method is adapted for clay-sand mixtures by incorporating the effect of changes in the threshold of motion and dimensions
- Clay can result in a reduction in the range of past water-surface wavelengths and water depths, which is largest for coarse sand

## Abstract

Wave ripples can provide valuable information on their formative hydrodynamic conditions in past subaqueous environments by inverting dimension predictors. However, these inversions do not usually take the mixed non-cohesive and cohesive nature of sediment beds into account. Recent experiments involving sand–kaolinite mixtures have demonstrated that wave-ripple dimensions and the threshold of motion are affected by bed clay content. Here, a clean-sand method to determine wave climate based on orbital ripple wavelength has been adapted to include the effect of clay and a consistent shear-stress threshold parameterisation. Based on present-day examples with known wave conditions, the results show that the largest clay effect occurs for coarse sand with median grain diameters over 0.45 mm. For a 7.4% volumetric clay concentration, the range of possible water-surface wavelengths and water depths can be reduced significantly, by a factor of three and four, respectively, compared to clean sand.

## Plain Language Summary

In shallow water, ripples form on the seabed under water-surface waves due to friction. Knowledge of this process allows preserved ripples to be used to infer past environmental conditions. Traditionally, the method of inferring past environments from wave ripples has only involved sand, despite mixtures of sand and sticky mud being more common in nature. Based on the results of recent mixed sand–mud experiments, the effect of including small amounts of mud in the analysis is shown to be an important modifying factor in determining past environments.

## 1 Introduction

Bed-surface structures in sediments and sedimentary rocks of past subaqueous environments provide important information on flow hydraulics (e.g. Collinson & Mountney, 2019). These structures tend to be classified on the basis of the presence or absence of cohesion in equivalent modern environments: (a) cohesive structures, associated with physical cohesion by clay particles and biological cohesion by extracellular polymeric substances (e.g. biofilms, Vignaga et al., 2013), where the bed is stabilised by cohesion between grains and sudden catastrophic failure may occur under high bed shear stress, e.g. during storms; and (b) non-cohesive bedforms (e.g. wave and current ripples: Wiberg & Harris, 1994; Baas, 1994), where grains can move individually and tend to respond more rapidly and continuously to changes in flow forcing (Perron et al., 2018). Examples of these types of bed-surface structure include roll-ups (Cuadrado, 2020) and non-cohesive wave ripples (e.g. Allen, 1981). Davies (2016) argued that the distinction between cohesive and non-cohesive sedimentary structures is artificial, as they represent end members of a spectrum, and thus predictions based on one classification may result in misinterpretations. This position is re-enforced by recent experiments that have shown how sandy bedforms can be affected by small amounts of biological and physical cohesion (Malarkey et al., 2015; Parsons et al., 2016; Wu et al., 2018; 2022). The consequence for wave ripples of physical cohesion associated with kaolin clay in the bed has been detailed by Wu et al. (2024). Building on the work of Allen (1981), Diem (1985) developed a clean-sand analytical method for the prediction of paleowave climate based on the dimensional measurement of wave ripples in the rock record (Aspler et al., 1994; Wetzel et al., 2003; Allen & Hoffman, 2005; Pochat & Van Den Driessche, 2011, Lamb et al., 2012). Here, Diem’s (1985) approach is adapted for sand–clay mixtures, using the synthesis proposed by Wu et al. (2024).

Diem's (1985) approach starts by determining the wave orbital diameter from the ripple wavelength, without requiring a specific wavelength predictor. Here, the formulation starts as Diem (1985) did, with linear wave theory and additional constraints based on threshold of motion and wave breaking. It will then return to the effect of clay on ripple-wavelength prediction and the threshold of motion. The importance of clay content is demonstrated with the use of present-day examples from the laboratory and field, where the wave conditions were known.

## 2 Diem's (1985) method

### 2.1 Linear wave theory

In linear wave theory, the dispersion relation and the wave-velocity amplitude,  $U_0$ , are

$$\sigma^2 = gk \tanh kh, \quad U_0 = \pi d_0 / T, \quad (1a,b)$$

where  $\sigma = 2\pi/T$ ,  $T$  is the wave period,  $g$  is the acceleration due to gravity ( $= 9.81 \text{ m s}^{-2}$ ),  $k = 2\pi/L$ ,  $L$  is the water-surface wavelength,  $h$  is the water depth,  $d_0$  is the orbital diameter ( $= H/\sinh kh$ ) and  $H$  is the wave height. The wave properties, characterised by eqs. (1a,b), are subject to two constraints:

#### 2.1.1 Threshold of motion

$U_t$ , the critical wave-velocity amplitude associated with the threshold of motion, is a function of  $d_0$  and  $D_{50}$ , the median grain diameter. For sediment movement  $U_0^2 > U_t^2$ , which when combined with eqs. (1a,b) gives

$$x < \tanh kh, \quad (2)$$

where  $x = L/L_{t\infty}$  and  $L_{t\infty} = \frac{1}{2}\pi g(d_0/U_t)^2$  is the deep-water surface wavelength corresponding to the threshold of motion.

#### 2.1.2 Wave breaking

According to Miche (1944), the wave-breaking criterion defines the maximum possible wave steepness as,  $H/L \leq 0.142 \tanh kh$ , which when combined with  $d_0$  and  $L_{t\infty}$  gives

$$x \geq A \cosh kh, \quad (3)$$

where  $A = d_0/0.142L_{t\infty} = U_t^2/(0.071\pi g d_0)$ . It will be shown below that  $A < \frac{1}{2}$ , so if  $A = \frac{1}{2}(U_t/U_m)^2$ , where  $U_m = (0.0355\pi g d_0)^{1/2}$  is the maximum wave-velocity amplitude ( $U_m > U_t$ ), then  $U_t < U_0 \leq U_m$  and from eq. (1b)  $\pi d_0/U_m \leq T < \pi d_0/U_t$ .

Eqs. (2) and (3) represent the range of possible conditions between threshold and wave breaking for the wave climate. The limits of these constraints can be found by combining eqs. (2) and (3) using the identity  $1 - \tanh^2 kh = \text{sech}^2 kh$ , such that the maximum and minimum in  $x$  satisfy the equation  $x^4 - x^2 + A^2 = 0$ , so that  $x_{\max, \min}$  are

$$x_{\max, \min} = [\frac{1}{2} \pm \frac{1}{2}(1 - 4A^2)^{1/2}]^{1/2}, \quad (4)$$

where  $A < 1/2$ , for there to be two distinct values. Here,  $x$  and  $kh$  are in the ranges  $x_{\min} \leq x < x_{\max}$  and  $\operatorname{arctanh} x < kh \leq \operatorname{arccosh}(x/A)$ , respectively.

Figure 1 shows  $kh$  versus  $x$  for the limiting single-value case where  $U_m^2 = U_t^2$  ( $A = 1/2$ ,  $x = 2^{-1/2}$  and  $kh = \operatorname{arctanh} 2^{-1/2} \sim 0.88$ ) from shallow water ( $kh \ll 1$ ) to deep water ( $kh \gg 1$ ). Figure 1 also shows the  $A = 1/4$  case ( $U_m^2 = 2U_t^2$ ), corresponding to typical above-threshold wave conditions. In the latter case, the shaded region in Figure 1 shows the allowable values of  $x$  ( $1/4 \cosh kh \leq x < \tanh kh$ ) and the dots mark  $x_{\max, \min} = 1/2(2 \pm 3^{1/2})^{1/2}$  and  $kh_{\max, \min} = \operatorname{arctanh}(x_{\max, \min})$ . The breaking-wave curves ( $x = A \cosh kh$ ) are concave downward and the threshold curve ( $x = \tanh kh$ ) is concave upward. Notice for the breaking-wave curves,  $x \rightarrow A$  for  $kh \ll 1$  and  $A$  also controls the slope for larger  $kh$ . In dimensional terms, the water-surface wavelength,  $L$ , is therefore limited by the threshold scale ( $L_{t\infty}$ ) and breaking-wave scale ( $AL_{t\infty}$ ) according to  $AL_{t\infty} < L \leq L_{t\infty}$ . Then, from eqs. (2) and (3), the range of  $h$  can be expressed as a function of  $L$  as

$$(L/2\pi)\operatorname{arctanh}(L/L_{t\infty}) \leq h \leq (L/2\pi)\operatorname{arccosh}(L/AL_{t\infty}). \quad (5)$$

## 2.2 The ripple predictor

Diem's (1985) central assumption is that the orbital diameter can be expressed in terms of an equilibrium ripple wavelength,  $\lambda_e$ , as

$$\lambda_e = \alpha_0 d_0, \quad (6)$$

where  $\alpha_0 = 0.65$ , based on Miller and Komar's (1980) experiments, provided that  $\lambda_e < 200$  mm ( $d_0 = 308$  mm). Above this limit, Diem (1985) proposed the use of Sleath's (1975) predictor. This arbitrary 200-mm limit represents the lower boundary of the suborbital and anorbital ranges, where the wavelength is dependent on both  $d_0$  and  $D_{50}$  for suborbital ripples and only dependent on  $D_{50}$  for anorbital ripples. However, while a value of  $\alpha_0$  in the range  $0.5 \leq \alpha_0 \leq 0.75$  in eq. (6) is widely accepted, there is little agreement in the literature on the precise nature of the orbital, suborbital, and anorbital limits. Wiberg and Harris (1994) defined orbital, suborbital and anorbital ripples by  $d_0/D_{50} \leq 1754$ ,  $1754 < d_0/D_{50} \leq 5587$  and  $d_0/D_{50} > 5587$ , respectively (Malarkey & Davies, 2003), whereas Mogridge et al. (1994) and Pedocchi and García (2009) argued the anorbital limit should have wave-period dependence. Provided that eq. (6) *does* hold, which is what will be assumed here, all quantities involving  $d_0$  can now be expressed in terms of  $\lambda_e$ .

## 3 Adaptions to Diem's (1985) method

### 3.1 Threshold of motion parameterisation

Based on Soulsby's (1997) critical threshold of motion for clean sand, Appendix A derives an expression for  $U_t^2$ , eq. (A2), such that  $U_t^2$ ,  $L_{t\infty}$  and  $AL_{t\infty}$  can be written

$$U_t^2 = B(gd_0^{0.52}D_{50}^{0.48}), \quad L_{t\infty} = \frac{\pi}{2B} \left( \frac{d_0^{1.48}}{D_{50}^{0.48}} \right), \quad AL_{t\infty} = \frac{d_0}{0.142}, \quad (7a,b,c)$$

where  $B = 3.653(s-1)\theta_0$ ,  $s$  is the relative density of sediment in water (eq. A1),  $\theta_0$  is the critical skin friction Shields parameter (eq. A1), and  $d_0 = \lambda_e/\alpha_0$  from eq. (6). Diem (1985) used Komar and Miller's (1973) mobility threshold prescription. Here, Soulsby's expression has been used, as it allows  $U_t^2$  to be directly related to  $\theta_0$  and it avoids the need for two different functional forms, for  $D_{50} < 0.5$  mm and  $D_{50} \geq 0.5$  mm (eqs. (B1) and (B2)).

### 3.2 Inclusion of the effect of clay

Wu et al. (2024) showed that the ratio of wavelength to orbital diameter,  $\alpha$ , which replaces  $\alpha_0$  in eq. (6), can be expressed as

$$\alpha = \alpha_0 \times \begin{cases} 1, & C_0 \leq C_{0m}, \\ 1 - 5.5(C_0 - C_{0m}), & C_0 > C_{0m}, \end{cases} \quad (8)$$

where  $\alpha_0$  is the clean-sand constant of proportionality ( $= 0.61$ ),  $C_0$  is the clay content in the bed and  $C_{0m} = 7.4\%$  is the minimum value of  $C_0$  where  $\alpha$  can change from  $\alpha_0$ , and  $\alpha = \frac{1}{2}\alpha_0$  for  $C_0 = 16.3\%$ . Whitehouse et al. (2000) showed that the threshold of motion is enhanced by the clay content according to

$$\theta_{0E} = \theta_0 B_\theta, \quad (9)$$

where  $\theta_0$  is the clean-sand threshold,  $B_\theta = 1 + P_\theta C_0$  and  $P_\theta$  is a constant that depends on the sediment properties. Based on their experiments, Wu et al. (2024) determined that  $P_\theta = 6.3$  for  $D_{50} = 0.143$  mm and  $P_\theta = 23$  for  $0.45 \leq D_{50} \leq 0.5$  mm (between these two ranges, it will be assumed that  $P_\theta$  can be linearly interpolated). Notice in eq. (9) that even small amounts of clay produce an enhancement which is strongly dependent on grain size.

Thus, the two main effects of including clay are that  $\alpha$  is reduced and  $\theta_{0E}$  is increased. Substituting eqs. (8) and (9), into eqs. (7a,b,c) gives  $U_t^2$ ,  $L_{t\infty}$  and  $AL_{t\infty}$  as

$$U_t^2 = B \left[ \frac{B_\theta}{\alpha^{0.52}} \right] (g \lambda_e^{0.52} D_{50}^{0.48}), \quad L_{t\infty} = \frac{\pi}{2B[B_\theta \alpha^{1.48}]} \left( \frac{\lambda_e^{1.48}}{D_{50}^{0.48}} \right), \quad AL_{t\infty} = \frac{\lambda_e}{0.142[\alpha]}, \quad (10a,b,c)$$

where  $\lambda_e$  is the mixed clay–sand ripple wavelength and only the square-bracketed quantity in each expression depends on  $C_0$ .

### 3.3 The method

The method begins with the determination of the ripple wavelength,  $\lambda_e$ , and bed-clay content,  $C_0$ . Once these have been determined, the following calculations are undertaken:

(i) Use  $\lambda_e$  and  $C_0$  in eqs. (10a,b,c), with  $\alpha$  and  $B_\theta$  given by eqs. (8) and (9), to determine  $U_t$ ,  $L_{t\infty}$  and  $AL_{t\infty}$

(ii) Use  $A$  in eq. (4) to determine  $x_{\max, \min}$ , so that  $x_{\min} \leq x \leq x_{\max}$

(iii) Use  $L = L_{t\infty} x$  to determine the range of  $h$  based on eq. (5) and  $U_t$  and  $U_m = (0.0355 \pi g \lambda_e / \alpha)^{1/2}$  to determine the ranges of  $U_0$  and  $T$ :  $U_t < U_0 < U_m$  and  $\pi \lambda_e / \alpha U_m < T < \pi \lambda_e / \alpha U_t$

## 4 Example cases

With specific examples from the rock record, Diem (1985) was able to show how local considerations and context could be used to further limit the theoretical ranges described in the previous section. Here, modern-day examples, where the wave properties are known, are used, so that attention can be focussed on the effect of clay on the theoretical ranges alone. The example cases correspond to clean, coarse-, medium- and fine-grained sand from the laboratory and field, and involve determining how wave conditions based on the measured ripples change if the clay content is varied in the range  $0 \leq C_0 \leq 16.3\%$ .

### 4.1 Wu et al. (2018), coarse-sand laboratory data

Wu et al. (2018) conducted a series of experiments involving a single-wave condition over a bed composed of well-sorted coarse sand,  $D_{50} = 0.496$  mm ( $\theta_0 = 0.032$ ), and varying clay content,  $0 \leq C_0 \leq 7.4\%$ . For the clean sand experiment ( $C_0 = 0\%$ ), the wave conditions were given by  $h = 0.6$  m,  $H = 0.16$  m and  $T = 2.49$  s ( $L = 5.62$  m), corresponding to  $d_0 = 0.223$  m. This experiment produced ripples with a wavelength  $\lambda_e = 278D_{50}$  (Wu et al., 2024). Figure 2a show the threshold and wave-breaking scales,  $L_{f\infty}$  and  $AL_{f\infty}$ , versus  $C_0$ .  $L_{f\infty}$ , which is smallest at  $C_0 = 7.4\%$ , has a much larger range than  $AL_{f\infty}$ , which is constant for  $C_0 \leq 7.4\%$  and then doubles up to  $C_0 = 16.3\%$ . Figure 2d shows the corresponding  $L$ - $h$  phase space, based on eq. (5), for the clay contents depicted in Figure 2a ( $C_0 = 0, 7.4$  and  $16.3\%$ ). Compared to the dimensionless  $x$ - $kh$  plot (Figure 1), the threshold curves are still concave downwards, but more exaggerated, and the breaking-wave curves are close to straight lines. The change in ranges is largely due to changes in  $L_{f\infty}$ . The reduction in range between the largest and smallest (corresponding to  $C_0 = 0\%$  and  $7.4\%$ ) is by a factor of 3 and 4 for the water-surface wavelength and water depth, respectively (Figure 2d). Notice that the actual surface wavelength and water depth ( $L = 5.62$  m,  $h = 0.6$  m) are within all three ranges. Figures 2a,d can be compared with Figures B1a,b to see the effect of using the Komar and Miller (1973) clean-sand mobility description for the threshold. This shows  $L_{f\infty}$  to be about 63% of its value in Figure 2a, because  $B = 0.21(s-1) = 0.34$  as opposed to  $3.653(s-1)\theta_0 = 0.19$ . Thus, using Diem's (1985) clean-sand mobility description underpredicts the range of water-surface wavelengths and heights in an absolute sense. In a relative sense, the change in the ranges of clay content is similar, because the powers of  $d_0$  and  $D_{50}$  are similar (eq. (B2), for  $D_{50} < 0.5$  mm, and eq. (10a)), but this will not be the case for  $D_{50} > 0.5$  mm. Also, the measured  $L$  and  $h$  are not within the  $C_0 = 7.4\%$  range (Figure B1b). As  $L$  and  $h$  are below the threshold curve, this would imply that ripples of this size are relict for this clay content. This is inconsistent with the experimental results, since Wu et al. (2024) showed no reduction in  $\lambda_e$  for  $C_0 \leq 7.4\%$ .

#### 4.2 Doucette (2000), medium-sand field data

Doucette's (2000) field measurements were taken on a microtidal beach of Wambro Sound (run 1) where  $h = 0.47$  m,  $H = 0.2$  m and  $T = 5.6$  s ( $L = 11.9$  m), corresponding to  $d_0 = 0.79$  m. The bed was composed of medium sand, with  $D_{50} = 0.22$  mm ( $\theta_0 = 0.045$ ), and the measured ripples had a wavelength of  $\lambda_e = 250$  mm. Since  $d_0/D_{50} = 3591$ , the ripples were in the suborbital range (see section 2.2), where the wavelength is dependent on both the orbital and grain diameters. Notice this wavelength is above Diem's (1985) 200-mm limit. The supporting information demonstrates that, whilst using Sleath's (1975) predictor for  $C_0 = 0$  produces a difference, it is similar to the other two example cases, which are below Diem's (1985) limit, and so is not considered significant. From interpolation,  $P_\theta$  in eq. (9) is determined to be 10. Figure 2b shows  $L_{f\infty}$  and  $AL_{f\infty}$  versus  $C_0$  and Figure 2e shows the  $L$ - $h$  phase space, for  $C_0 = 0, 7.4$  and  $16.3\%$ . These reveal similar behaviour to that of the coarse-grained sand case, but less extreme: in Figure 2b,  $L_{f\infty}$  is still at its minimum at  $C_0 = 7.4\%$  and  $AL_{f\infty}$  shows the same enhancement as in Figure 2a. The reduction in range between the largest and smallest ( $C_0 = 0\%$  and  $7.4\%$ ) is by a factor of 2 for both the water-surface wavelength and water depth (Figure 2e). Again, the actual surface wavelength and water depth ( $L = 11.9$  m,  $h = 0.47$  m) are within all three ranges.

#### 4.3 Boyd et al. (1988), fine-sand field data

Boyd et al.'s (1988) field measurements were undertaken about 1 km from Martinique Beach on the Atlantic coast of Nova Scotia during a period of relative calm (day 167, hour 9) where  $h = 10$

m,  $H = 0.5$  m and  $T = 6.2$  s ( $L = 50.7$  m), corresponding to  $d_0 = 0.32$  m. The bed was composed of well-sorted fine sand, with  $D_{50} = 0.11$  mm ( $\theta_0 = 0.076$ ), and the measured ripples had a wavelength of  $\lambda_e = 180$  mm.  $d_0/D_{50} = 2873$  puts the ripples into the suborbital range. Assuming that  $P_0$  in eq. (9) is the same as for 0.143 mm ( $P_0 = 6.3$ ), Figure 2c shows  $L_{t\infty}$  and  $AL_{t\infty}$  versus  $C_0$  and Figure 2f shows the  $L$ - $h$  phase space, for  $C_0 = 0, 7.4$  and 16.3%.  $L_{t\infty}$  in Figure 2c is still at its minimum at  $C_0 = 7.4\%$ , but, because of far weaker clay enhancement of the threshold for fine sands in eq. (9),  $L_{t\infty}$  is largest for  $C_0 = 16.3\%$ . In Figure 2f, the measured water-surface wavelength and water depth ( $L = 50.7$  m,  $h = 10$  m) are below the threshold curve and outside the range for the  $C_0 = 0$  and 7.4% clay contents, and just above the threshold curve and within range for  $C_0 = 16.3\%$ , because, unlike the previous cases,  $C_0 = 16.3\%$  produces the largest  $L_{t\infty}$ . Since there was little clay at the field site, the wave conditions were probably below threshold, implying that the observed ripples were relict. This is supported by the fact that Boyd et al.'s (1988) previous observation at day 167, hour 3, showed the same wavelength and no ripple migration. The reduction in range between the largest and smallest ( $C_0 = 16.3\%$  and 7.4%) is again by a factor of 2 for both the water-surface wavelength and water depth (Figure 2f).

## 5 Discussion

The range of  $L$  shown in Figure 2 is largely controlled by  $L_{t\infty}$ , so it is of interest to determine how the change in clay content affects  $L_{t\infty}$ , eq. (10b), compared to the original clean-sand Diem method using Komar and Miller (1973),  $L_{t\infty\text{KM}}$ , eq. (B2) with  $C_0 = 0\%$ . The net effect is shown as a ratio in Figure 3 for  $C_0 = 0, 7.4$  and 16.3% and  $0.1 \leq D_{50} \leq 0.8$  mm, for the approximate limits in the range of  $\lambda_e/D_{50}$  of 250 and 1,000. There are two competing effects: the reduction because of clay content (Figure 2) and the increase because of using Soulsby's (1997) threshold condition rather than Komar and Miller's (1973). Figure 3 shows a discontinuity for clean sand at  $D_{50} = 0.5$  mm as a result of eq. (B2), leading to the largest difference ( $L_{t\infty}$  is increased by up to 161% for  $\lambda_e/D_{50} = 250$ ), which decreases with increasing  $\lambda_e/D_{50}$  (although Diem's (1985) method has rarely been applied for  $D_{50} > 0.5$  mm). Otherwise for  $D_{50} \leq 0.19$  mm,  $L_{t\infty}$  is reduced by up to 36%, and for  $0.19 < D_{50} \leq 0.5$  mm,  $L_{t\infty}$  is increased by up to 64%. For  $C_0 = 7.4\%$ ,  $L_{t\infty}$  is consistently decreased by between 35 and 56%, and for  $C_0 = 16.3\%$ ,  $L_{t\infty}$  varies only slightly (increased by up to 14%, for  $0.12 \leq D_{50} \leq 0.37$  mm, and otherwise reduced by up to 15%). The absence of a discontinuity in the present formulation, compared to Diem's (1985) original formulation, is clearly preferable. Also, the net effect of the clay on  $L_{t\infty}$  will be stronger for smaller than for larger clay contents.

It is important to clarify how a representative clay content,  $C_0$ , for the ripples should be determined. In the modern environment this usually involves measuring  $C_0$  below the active layer (below trough level), as efficient winnowing often removes clay from the body of the ripples during development (Wu et al., 2022). In the geological record, clay content in deposits should be based on primary clay minerals and diagenetic alterations for which it can be established that the original mineral was part of the primary clay fraction.

## 6 Conclusions

Preserved sedimentary bedforms provide important information for reconstructing past hydraulics in subaqueous environments by inverting bedform predictors, but this is usually based exclusively on non-cohesive sand. The present work incorporates the effects of sand-clay mixtures on bedforms, using the experimental results of Wu et al. (2024) in the non-cohesive



inversion method of Diem (1985). Based on wave breaking and threshold of motion limitations, Diem's (1985) approach results in ranges for wave conditions. Here we have shown that the inclusion of as little as 7.4% clay in the most extreme case of coarse sand,  $D_{50} \geq 0.45$  mm, reduces the possible ranges of water-surface wavelengths and water depths by factors of 3 and 4, respectively. For fine sand, the ranges are reduced by a factor of two. In short, not accounting for the modifying effect of clay in ripple growth and equilibrium geometries, may lead to underestimating the prevailing flow conditions if clay is present.

## Appendix A: Determination of $U_t^2$ based on Soulsby (1997)

According to Soulsby (1997), the Shields parameter for the critical threshold of motion of clean sand is

$$\theta_0 = \frac{0.3}{1+1.2D_*} + 0.055(1-e^{-0.02D_*}), \quad (A1)$$

where  $D_* = [(s-1)g/\nu^2]^{1/3} D_{50}$ ,  $s = \rho_s/\rho$ ,  $\rho_s$  and  $\rho$  are the water and sediment densities and  $\nu$  is the kinematic viscosity ( $\sim 1 \text{ mm}^2 \text{ s}^{-1}$ ). For waves,  $\theta_0 = f_w U_t^2 / 2(s-1)gD_{50}$ , where  $f_w = 1.39(6d_0/D_{50})^{-0.52}$  is the skin friction factor (Soulsby et al., 1993). Rearranging the  $\theta_0$  wave expression gives  $U_t^2$  as

$$U_t^2 = B(gd_0^{0.52} D_{50}^{0.48}), \quad (A2)$$

where  $B = 6^{0.52}(s-1)\theta_0/0.695 = 3.653(s-1)\theta_0$ . Eq. (A2) can be compared with eq. (B1).

## Appendix B: Diem's (1985) threshold of motion constraint

Diem (1985) used the Komar & Miller (1973) expression for  $U_t^2$ , namely

$$U_t^2 = (s-1)g \times \begin{cases} 0.21(d_0^{0.5} D_{50}^{0.5}), & D_{50} < 0.5 \text{ mm}, \\ 0.46\pi(d_0^{0.25} D_{50}^{0.75}), & D_{50} \geq 0.5 \text{ mm}, \end{cases} \quad (B1)$$

such that with the inclusion of clay  $L_{t\infty} = \pi g d_0^2 / 2B_\theta U_t^2$ ,  $d_0 = \lambda_e/\alpha$  and  $B_\theta$  and  $\alpha$  are given by eqs. (8) and (9), giving  $L_{t\infty}$  as

$$L_{t\infty} = \frac{\pi}{2(s-1)} \times \begin{cases} \frac{1}{0.21[B_\theta \alpha^{1.5}]} \left( \frac{\lambda_e^{1.5}}{D_{50}^{0.5}} \right), & D_{50} < 0.5 \text{ mm}, \\ \frac{1}{0.46\pi[B_\theta \alpha^{1.75}]} \left( \frac{\lambda_e^{1.75}}{D_{50}^{0.75}} \right), & D_{50} \geq 0.5 \text{ mm}, \end{cases} \quad (B2)$$

and  $AL_{t\infty}$  as  $\lambda_e/0.142[\alpha]$  remains the same. Figure B1 shows the effect of this parameterisation of the threshold of motion for the first example case of Wu et al. (2018) depicted in Figures 2a,d. Unlike Figure 2d, the measured values of  $h$  and  $L$  are outside the range predicted for  $C_0 = 7.4\%$ .

## Acknowledgments

The participation of JM, EMP, XW, RF, JHB and DRP was made possible thanks to funding by the European Research Council under the European Union's Horizon 2020 research and innovation program (grant no. 725955). Participation of RF was also supported by the Leverhulme Trust, Leverhulme Early Career Researcher Fellowship (grant ECF-2020-679).

## Open Research

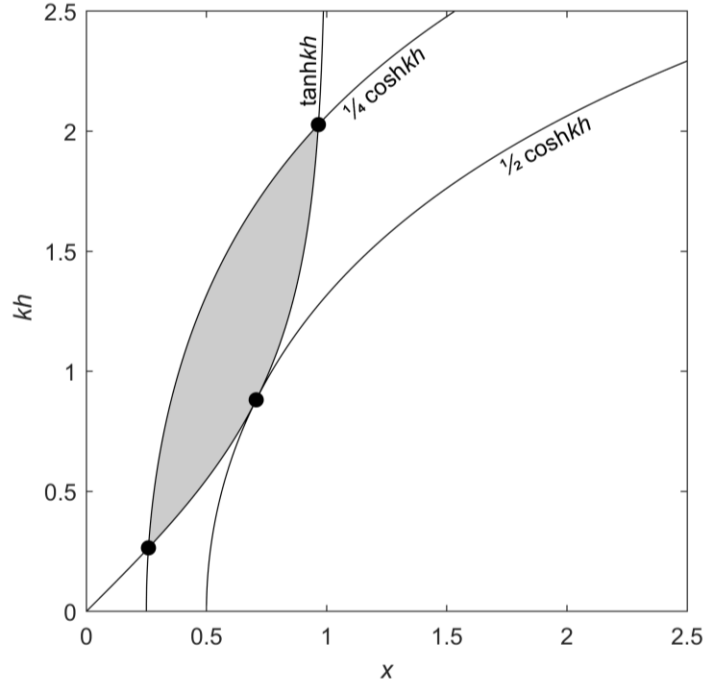
Eqs. (8) and (9) are from Wu et al. (2024), which has its own open-access policy.

## References

- Allen, P.A. (1981). Some guidelines in reconstructing ancient sea conditions from wave ripplemarks. *Marine Geology*, 43, 59–67. [https://doi.org/10.1016/0025-3227\(81\)90176-6](https://doi.org/10.1016/0025-3227(81)90176-6)
- Allen, P.A., & Hoffman, P.F. (2005). Extreme winds and waves in the aftermath of a Neoproterozoic glaciation. *Nature*, 433, 123–127. <https://doi.org/10.1038/nature03176>
- Aspler, L.B., Chiarenzelli, J.R., & Bursey, T.L. (1994). Ripple marks in quartz arenites of the Hurwitz group, Northwest territories, Canada: evidence for sedimentation in a vast, early Proterozoic, shallow, fresh-water lake. *Journal of Sedimentary Research*, A64, 282–298. <https://doi.org/10.1306/D4267D7F-2B26-11D7-8648000102C1865D>
- Baas, J.H. (1994). A flume study on the development and equilibrium morphology of current ripples in very fine sand. *Sedimentology*, 41, 185–209. <https://doi.org/10.1111/j.1365-3091.1994.tb01400.x>
- Boyd, R., Forbes, D.L., & Heffler, D.E. (1988). Time-sequence observations of wave-formed sand ripples on an ocean shoreface. *Sedimentology*, 35, 449–464. <https://doi.org/10.1111/j.1365-3091.1988.tb00997.x>
- Collinson, J., & Mountney, N. (2019). *Sedimentary structures* (Fourth Edition), Edinburgh, UK: Dunedin Academic Press. ISBN 1780460627
- Cuadrado, D.G. (2020). Geobiological model of ripple genesis and preservation in a heterolithic sedimentary sequence for a supratidal area. *Sedimentology*, 67, 2747–2763. <https://doi.org/10.1111/sed.12718>
- Davies, N.S., Liu, A.G., Gibling, M.R., & Miller, R.F. (2016). Resolving MISS conceptions and misconceptions: A geological approach to sedimentary surface textures generated by microbial and abiotic processes. *Earth-Science Reviews*, 154, 210–246. <https://doi.org/10.1016/j.earscirev.2016.01.005>
- Diem, B. (1985). Analytical method for estimating palaeowave climate and water depth from wave ripple marks. *Sedimentology*, 32, 705–720. <https://doi.org/10.1111/j.1365-3091.1985.tb00483.x>
- Doucette, J.S. (2000). The distribution of nearshore bedforms and effects on sand suspension on low-energy, micro-tidal beaches in Southwestern Australia. *Marine Geology*, 165, 41–61. [https://doi.org/10.1016/S0025-3227\(00\)00002-5](https://doi.org/10.1016/S0025-3227(00)00002-5)
- Komar, P.D., & Miller, M.C. (1973). The threshold of sediment movement under oscillatory water waves. *Journal of Sedimentary Petrology*, 43, 1101–1110. <https://doi.org/10.1306/74D7290A-2B21-11D7-8648000102C1865D>
- Lamb, M.P., Fischer, W.W., Raub, T.D., Perron, J.T., & Myrow, P.M. (2012). Origin of giant wave ripples in snowball Earth cap carbonate. *Geology*, 40, 827–830. <https://doi.org/10.1130/G33093.1>
- Malarkey, J., Baas, J.H., Hope, J.A., Aspden, R.J., Parsons, D.R., Peakall, J., Paterson, D.M., Schindler, R.J., Ye, L., Lichtman, I.D., Bass, S.J., Davies, A.G., Manning, A.J., & Thorne, P.D. (2015). The pervasive role of biological cohesion in bedform development. *Nature communications*, 6, 6257. <https://doi.org/10.1038/ncomms7257>
- Malarkey, J., & Davies, A.G. (2003) A non-iterative procedure for the Wiberg and Harris (1994) oscillatory sand ripple predictor. *Journal of Coastal Research*, 19, 738–739. <http://www.jstor.org/stable/4299210>
- Miche, R. (1944). Mouvements ondulatoires de la mer en profondeur constante ou décroissante. *Annales des Ponts et Chaussées*, 19, 369–406. <https://repository.tudelft.nl/islandora/object/uuid%3A6fceed55-d71b-4e3e-a94f-98ff17cb8f91>

- Miller, M.C., & P.D. Komar (1980). Oscillation sand ripples generated by laboratory apparatus. *Journal of Sedimentary Petrology*, 50, 173–182. <https://doi.org/10.1306/212F799B-2B24-11D7-8648000102C1865D>
- Mogridge, G.R., Davies, M.H., & Willis, D.H. (1994). Geometry prediction for wave-generated bedforms. *Coastal Engineering*, 22, 255–286. [https://doi.org/10.1016/0378-3839\(94\)90039-6](https://doi.org/10.1016/0378-3839(94)90039-6)
- Parsons, D.R., Schindler, R.J., Hope, J.A., Malarkey, J., Baas, J.H., Peakall, J., Manning, A.J., Ye, L., Simmons, S., Paterson, D.M., Aspden, R.J., Bass, S.J., Davies, A.G., Lichtman, I.D., & Thorne, P.D. (2016). The role of biophysical cohesion on subaqueous bed form size. *Geophysical Research Letters*, 43, 1566–1573. <https://doi.org/10.1002/2016GL067667>
- Pedocchi, F., & García, M.H. (2009). Ripple morphology under oscillatory flow: 2. Experiments, *Journal of Geophysical Research*, 114, C12015. <https://doi.org/10.1029/2009JC005356>
- Perron, J.T., Myrow, P.M., Huppert, K.L., Koss, A.R., & Wickert, A.D. (2018). Ancient record of changing flows from wave ripple defects. *Geology*, 46, 875–878. <https://doi.org/10.1130/G45463.1>
- Pochat, S., & Van Den Driessche, J. (2011). Filling sequence in Late Paleozoic continental basins: A chimera of climate change? A new light shed given by the Graissessac–Lodève basin (SE France). *Palaeogeography, Palaeoclimatology, Palaeoecology*, 302, 170–186. <https://doi.org/10.1016/j.palaeo.2011.01.006>
- Sleath, J.F.A. (1975). A contribution to the study of vortex ripples. *Journal of Hydraulic Research*, 13, 315–328. <https://doi.org/10.1080/00221687509499705>
- Soulsby, R. (1997). *Dynamics of Marine Sands: A Manual for Practical Applications*, London UK: Thomas Telford. ISBN 072772584X
- Soulsby, R.L., Hamm, L., Klopman, G., Myrhaug, D., Simons, R.R., & Thomas, G.P. (1993). Wave–current interactions within and outside the bottom boundary layer. *Coastal Engineering*, 21, 41–69. [https://doi.org/10.1016/0378-3839\(93\)90045-A](https://doi.org/10.1016/0378-3839(93)90045-A)
- Vignaga, E., Sloan, D.M., Luo, X., Haynes, H., Phoenix, V.R., & Sloan, W.T. (2013). Erosion of biofilm-bound fluvial sediments. *Nature Geoscience*, 6, 770–774. <https://doi.org/10.1038/ngeo1891>
- Wetzel, A., Allenbach, R., & Allia, V. (2003). Reactivated basement structures affecting the sedimentary facies in a tectonically “quiescent” epicontinental basin: an example from NW Switzerland. *Sedimentary Geology*, 157, 153–172. [https://doi.org/10.1016/S0037-0738\(02\)00230-0](https://doi.org/10.1016/S0037-0738(02)00230-0)
- Whitehouse, R., Soulsby, R., Roberts W., & Mitchener, H. (2000). *Dynamics of estuarine muds: A Manual for Practical Applications*, London UK: Thomas Telford. ISBN 0727728644
- Wiberg, P.L., & Harris, C.K. (1994). Ripple geometry in wave-dominated environments. *Journal of Geophysical Research*, 99(C1), 775–789. <https://doi.org/10.1029/93JC02726>
- Wu, X., Baas, J.H., Parsons, D.R., Eggenhuisen, J., Amoudry, L., Cartigny, M., McLelland, S., Mouazé, D., & Ruessink, G. (2018). Wave ripple development on mixed clay–sand substrates: Effects of clay winnowing and armoring. *Journal of Geophysical Research: Earth Surface*, 123, 2784–2801. <https://doi.org/10.1029/2018JF004681>
- Wu, X., Fernández, R., Baas, J.H., Malarkey, J., & Parsons, D.R. (2022). Discontinuity in equilibrium wave–current ripple size and shape and deep cleaning associated with cohesive sand–clay beds. *Journal of Geophysical Research: Earth Surface*, 127, e2022JF006771. <https://doi.org/10.1029/2022JF006771>

364 Wu, X., Malarkey, J., Fernández, R., Baas, J.H., Pollard, E., & Parsons, D.R. (2024). Influence  
365 of cohesive clay on wave-current ripple dynamics captured in a 3D phase diagram. *Earth Surface*  
366 *Dynamics*, 12, 231–247. <https://doi.org/10.5194/esurf-12-231-2024>



367 **Figure 1**  $kh$  versus  $x$  ( $L/L_{\infty}$ ) for the limiting case of  $A = 1/2$  and also  $A = 1/4$ . Dots correspond to  $x$   
 368  $= 2^{-1/2}$  and  $kh = \text{arctanh} 2^{-1/2}$ , for  $A = 1/2$ ;  $x_{\text{max,min}} = 1/2(2 \pm 3^{1/2})^{1/2}$  and  $kh_{\text{max,min}} = \text{arctanh}[x_{\text{max,min}}]$ , for  $A$   
 369  $= 1/4$ , and shading represents allowable values of  $x$  and  $kh$  for  $A = 1/4$  ( $1/4 \cosh kh \leq x \leq \tanh kh$ ).

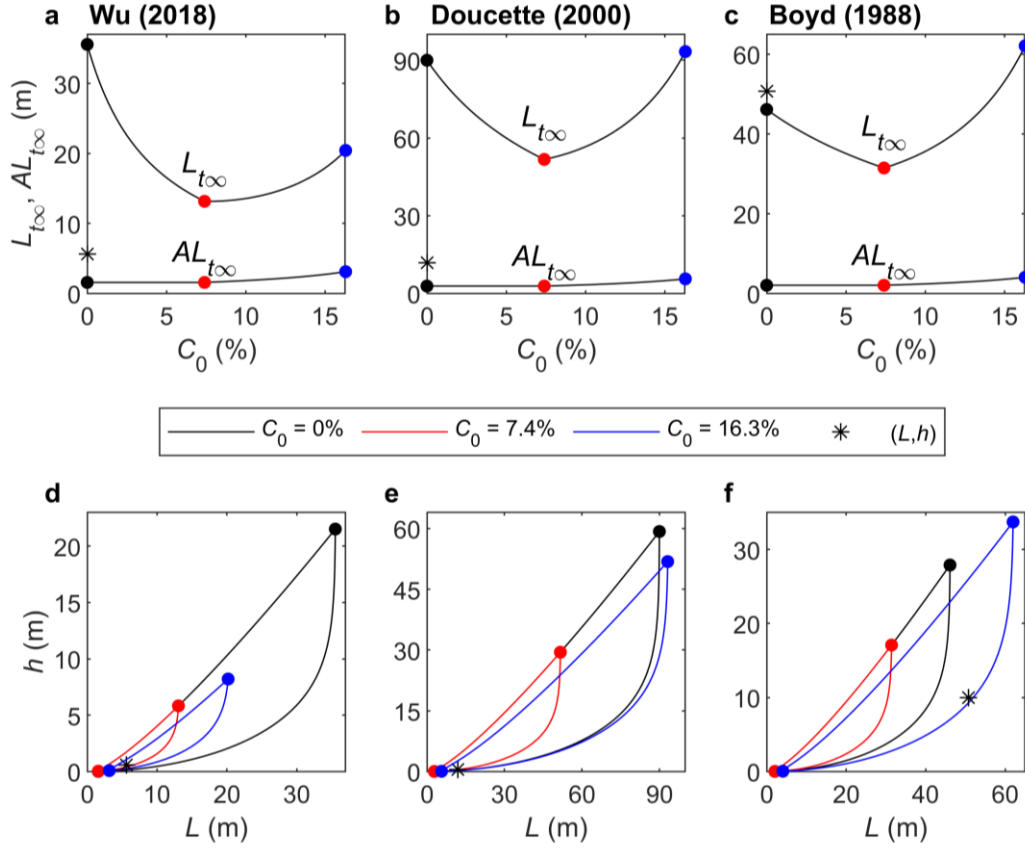


**Figure 2** (a,b,c) Threshold,  $L_{t\infty}$ , and wave-breaking,  $AL_{t\infty}$ , scales, eqs. (10b,c), versus  $C_0$  and (d,e,f)  $L$ - $h$  phase space from eq. (5), showing the different ranges for  $C_0 = 0, 7.4$  and  $16.3\%$  and the measured  $L$  and  $h$ . For (a,d) Wu et al. (2018),  $\lambda_e = 278D_{50}$ ,  $D_{50} = 0.496$  mm,  $\theta_0 = 0.032$ ,  $L = 5.62$  m and  $h = 0.6$  m; for (b,e) Doucette (2000),  $\lambda_e = 250$  mm,  $D_{50} = 0.22$  mm,  $\theta_0 = 0.045$ ,  $L = 11.9$  m and  $h = 0.47$  m, and for (c,f) Boyd et al. (1988),  $\lambda_e = 180$  mm,  $D_{50} = 0.11$  mm,  $\theta_0 = 0.076$ ,  $L = 50.7$  m and  $h = 10$  m. Legend applies to d,e,f; colours in a,b,c are consistent with the legend.

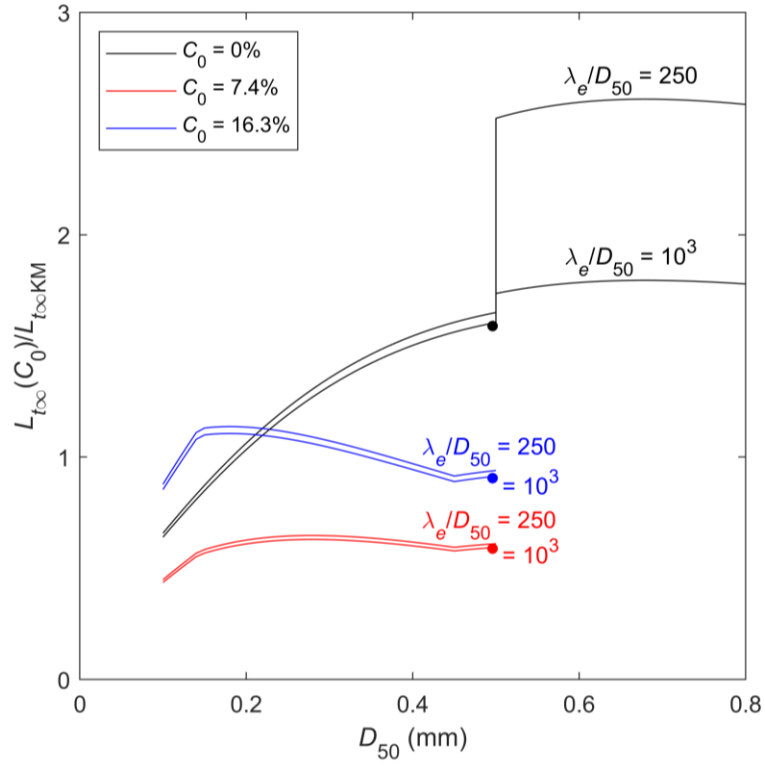


**Figure 3** Relative size of  $L_{t\infty}(C_0)$  from eq. (10b) normalised by the clean-sand  $L_{t\infty}$  from eq. (B2),  $L_{t\infty KM}$ , for  $C_0 = 0, 7.4$  and  $16.3\%$ .  $\lambda_e/D_{50} = 250$  and  $1000$ , and the dots correspond to Wu et al.'s (2018) clean-sand experiment in Figure 2a.

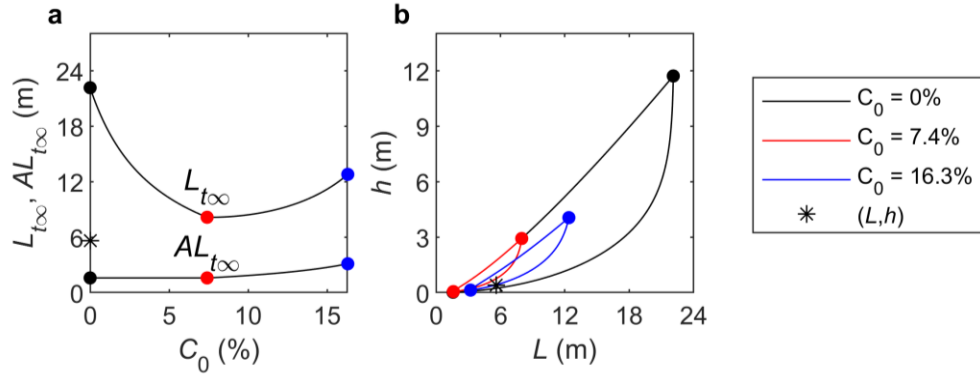


**Figure B1** (a) Threshold,  $L_{t\infty}$ , and wave-breaking scales,  $AL_{t\infty}$ , eqs. (B2) and (10c), versus  $C_0$  and (b)  $L-h$  phase space from eq. (5) showing the different ranges for  $C_0 = 0, 7.4$  and  $16.3\%$  and the measured  $h$  and  $L$  for Wu et al. (2018),  $\lambda_e = 278D_{50}$ ,  $D_{50} = 0.496$  mm,  $h = 0.6$  m and  $L = 5.62$  m.